ASME Journal of Fluids Engineering
Online journal at:
https://asmedigitalcollection.asme.org/fluidsengineering

Experimental Study of Characteristics of Boundary Layer Flows With Pressure Shielding

Chenguang Yuan
The State Key Laboratory of Nonlinear Mechanics, Institute of Mechanics Chinese Academy of Sciences, Beijing 100190, China

Duo Xu[1]
The State Key Laboratory of Nonlinear Mechanics, Institute of Mechanics Chinese Academy of Sciences, Beijing 100190, China;
School of Engineering Sciences, University of Chinese Academy of Sciences, Beijing 100049, China
e-mail: duo.xu@imech.ac.cn

In this study, boundary layer flows over a flat plate with a canopy of an array of rods are experimentally investigated with particle image velocimetry (PIV) measurements. The experiments were carried out in a liquid tunnel, where the refractive index of the transparent liquid is matched with that of transparent rods in the array. The statistics of the velocity data at multiple planes show the change of the flow patterns produced by the rod array. The pressure field was calculated from the velocity data through solving the pressure Poisson equation. The power spectral density of the pressure fluctuations, quantifying the sound pressure level, shows that the rod array causes the attenuation of the pressure fluctuations both below and above the rod array. The characteristic flow patterns altered by the rod array were examined by the dynamic mode decomposition. The uncertainty of the measurements was discussed. [DOI: 10.1115/1.4062519]

Introduction

Flow induced noise is widespread with often nontrivial negative impact in engineering applications. For instance, in commercial aviation, the noise from flight engines has attracted long time attention, given that the airframe noise directly affects the human activities in both airports and their neighboring areas. In the meanwhile, attempts on reducing airframe noise have been raised since 1970s [1]. One technical route for the noise reduction is bio-inspired, e.g., from owls, given that during its predation an owl keeps its flight silent to approach its prey. Given this, Lilley [2] proposed to investigate the physical mechanism of owl's silent flight for advancing the design on reducing the airframe noise. In the early study of the silent flight of owls, Graham [3] proposed that three potential structures (i.e., the leading edge comb, the trailing edge fringe and the downy upper surface) are associated with minimizing the airframe noise. Hersh et al. [4] found that the airframe noise can be attenuated by serration structures on a leading edge of an airfoil, which also can improve the design for silent airfoils of wind turbines [5] and was proposed to be conducive to the noise reduction in contra-rotating open rotor [6]. Jaworski and Peake [7,8] applied theoretical analysis to the porous trailing edge, and confirmed the effect of the porous medium on the noise attenuation.

Recently, in the experimental study of turbulent boundary layer over a flat plate, Clark et al. [9] investigated the turbulence generated noise, which is reduced by using two bio-inspired structures, i.e., the weaved-fiber canopy and the unidirectional canopy. The latter is composed of an array of strings in parallel to the main flow direction, and the strings are suspended above a flat plate by mounting their ends on two lumps in the upstream and downstream, respectively. Their experiment was conducted in an anechoic wind tunnel, and the pressure was measured by microphones flush mounted at the flat surface and by the microphones in far field. They found that this string array can attenuate the pressure fluctuation in both near and far fields. In a follow-up study, Gonzalez et al. [10] replaced the strings in the canopy with steel rods. The array of rods was mounted in form of cantilever through fixing the downstream ends of the rods into a supporter (with airfoil cross section) and left the upstream end free of mounting. They proposed that the attenuation of surface pressure fluctuation in low and high frequency is attributed to the shear sheltering and the dissipation mechanism, respectively. For further insights into the mechanisms, in the same study, Reynolds–averaged Navier–Stokes (RANS) simulations of the same flow was performed with the $k-\varepsilon$ turbulence model for the closure of the governing equations. They numerically examined the flow structures altered by the rod-array canopy and attempted advancing the understanding of the mechanism of the noise reduction from the velocity fields.

Studying the characteristic flow structures can offer insights for better understanding the mechanisms in the pressure shielding, and more importantly this can provide guidance for designing the alternative pressure shielding structures in practical applications. The RANS simulations can provide accurate mean flow field, but give much less precise fluctuation velocity fields, which are closely determined by the performance of the turbulence models [11]. This is particular the case for flows of anisotropic structures [12], e.g., the characteristic patterns in the canopy flow of the pressure shielding. Without needs for turbulence models, experimental measurements of the flow via particle image velocimetry (PIV), on the other hand, can provide better details into the featured velocity fields. Benefited by its nonintrusive nature, PIV can measure the canopy flows of the pressure shielding without affecting the flows. This is particularly necessary, given that unsteady flows additionally caused by intrusive measurement techniques may affect the pressure field that is associated with the generation of the near- and far-field noise.

[1]Corresponding author.

Contributed by the Fluids Engineering Division of ASME for publication in the Journal of Fluids Engineering. Manuscript received November 9, 2022; final manuscript received April 30, 2023; published online July 21, 2023. Assoc. Editor: Stefan aus der Wiesche.

However, even though, applying PIV measurements in this flow is challenging in practice, given the unavoidable light reflections at the walls in the very small gaps between the rod array and the plate surface, and importantly the view blocking by the canopy array.

In this study, we carried out PIV measurements of the boundary layer flow over a flat plate with an array of rods (the same structure configuration as in Ref. [10]). The experiment was carried out in a liquid tunnel, where the refractive index of the transparent liquid and that of the transparent rod array are matched. This arrangement avoids the view-blocking of the camera for employment of the PIV measurement within the rod array. The rest of the paper is organized as follows. The experiment details are introduced first. Then, the measured velocity fields, the velocity spectra and the calculated pressure field by the PIV velocity data, as well as the analysis of the feature flow structures through dynamic mode decomposition are presented. The conclusion is drawn at last.

Methodology

Experimental Setup. The experiment was conducted in a liquid tunnel which is sketched in Fig. 1(*a*). The fluid is driven by a centrifugal pump to flow from left to right in the test section (marked by an arrow). The mean velocity in the test section was measured by the PIV measurement when the test section was free of models, and in the meanwhile the value of the flowmeter was recorded for selfexamination. The test section, made of polymethyl methacrylate (PMMA) plates, has a length of 500 mm and a square cross section of $100 \times 100\,\text{mm}^2$. In the contraction, a grid mesh was installed to provide approximately uniform turbulence fluctuations in space.

To provide nonblocking views of the flow fields, the rods used in this study were made of transparent borosilicate glass, which has a nominal refractive index of about 1.47. The water was mixed with Sodium Iodide (NaI) to match the refractive index of the glass rods. To calibrate the refractive index matching, a few short glass rods were laid on the bottom of a beaker filled with water, and the beaker was placed on a piece of newspaper. NaI was gradually added into a beaker and mixed for a few minutes until that the NaI was fully dissolved. This procedure was repeated until when the scripts on the newspaper can be seen through the glass rods with minimized distortions (justified by eye). The refractive index of the solution was measured to be 1.469 in a refractometer, very close to the nominal value of the glass rods. The well-mixed NaI solution in this concentration was used in the liquid tunnel. The density and the dynamic viscosity of the NaI solution in experiments is $\rho = 1711.419\,\text{kg}\cdot\text{m}^{-3}$ and $\mu = 1.863 \times 10^{-3}\,\text{Pa}\cdot\text{s}$ for the mass concentration of NaI [13], which gives the kinematic viscosity of the fluid $\nu = 1.09 \times 10^{-6}\,\text{m}^2/\text{s}$. Given the flow condition and property of the working fluid, the compressibility of the flow is not expected and considered in this study.

The rod array is composed of seven rods with identical spanwise intervals, and the rods were aligned along the main flow direction in parallel, as shown in Figs. 1(*c*) and 1(*e*). The diameter of the rods is $d = 5\,\text{mm}$, given the consideration of the structure strength for the glass material, although smaller diameter is preferred. The rods were mounted in a supporter with the cross section in shape of an airfoil, modified from the NACA-0017. The supporter was made of steel and coated with black paint to minimize light reflection. The height of the array of the rods from the top surface of the flat plate can be changed by adjusting the supporter. The flat plate in length of approximately 490 mm, made of PMMA, was placed along the flow streamwise direction. The leading and the trailing edge of the plate were wedged. The flat plate was mounted to the inner side-wall of the test section.

In this study, the leading front of the rod array was placed $L = 250\,\text{mm}$ downstream from the leading edge of the flat plate, which was located at the exit of the contraction section. The mean flow speed U_∞ is $0.23\,\text{m/s}$ to avoid breaking the glass rods, and correspondingly the Reynolds number $\text{Re}_x = U_\infty L/\nu = 5.3 \times 10^4$ at $x/h = 0$. Mesh grids were used in the contraction and the exit of the test section to increase the background turbulence intensity. The mean velocity profile, obtained from the PIV measurements, is shown in Fig. 2(*a*). Given by approximate 0.99 of the mean velocity, the thickness of the turbulent boundary layer is $\delta \approx 9\,\text{mm}$ at the leading front of the rods ($x/h = 0$), while $\delta(x)$ is approximately follows the curve of turbulent flow [14,15]. Without the rod array (the counterpart case), the spectra of the streamwise fluctuation velocity is shown in Fig. 2(*c*), and it is obtained using the time series of the PIV velocity measurements with Hanning filtering operation following the method in Ref. [16] at $(x/h, y/h) = (0, 1.4)$. At the same location, the estimated dissipation is about $1.2 \times 10^3\,\text{mm}^2/\text{s}^3$ taking the local isotropy assumption in Ref. [17]. Correspondingly, the estimated Taylor lengthscale, Kolmogorov timescale and lengthscale are about 2.32 mm, 0.03 s, and 0.18 mm , respectively, and the latter is slightly smaller than the spatial resolution of the PIV measurements so that the dissipation is expected to be

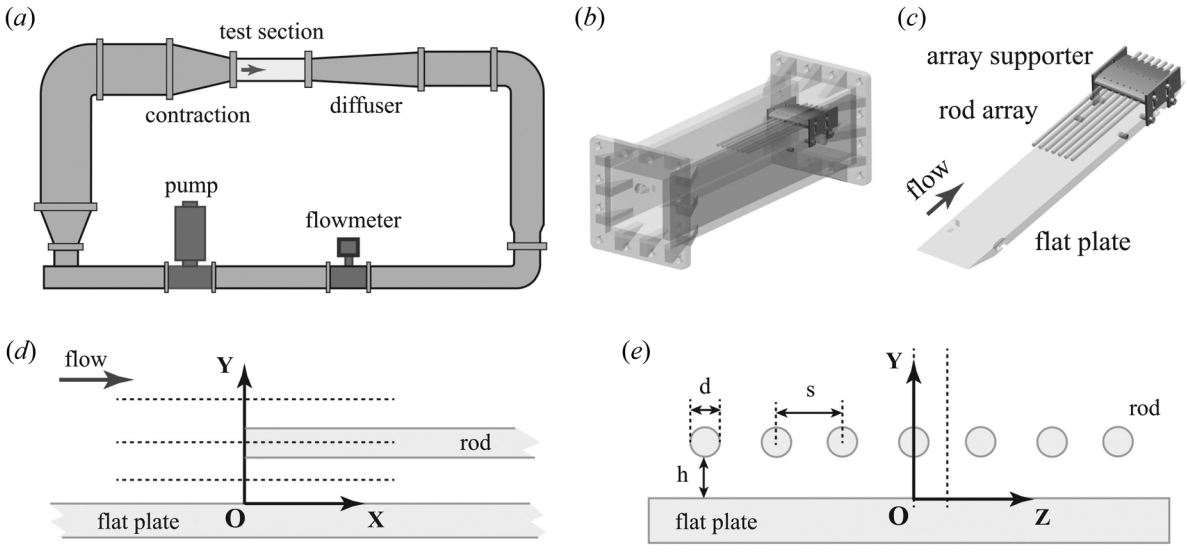

Fig. 1 (*a*) Sketch of facility and an arrow indicates the flow direction; (*b*) The test section including the experimental setup; (*c*) Three dimensional rendering of the experimental setup; (*d*) Sketch of the setup from the side view, and three dot lines mark the measurement planes; (*e*) Sketch of the setup from the perspective of the flow direction (i.e., flow into the page), and the two dot lines mark the measurement planes

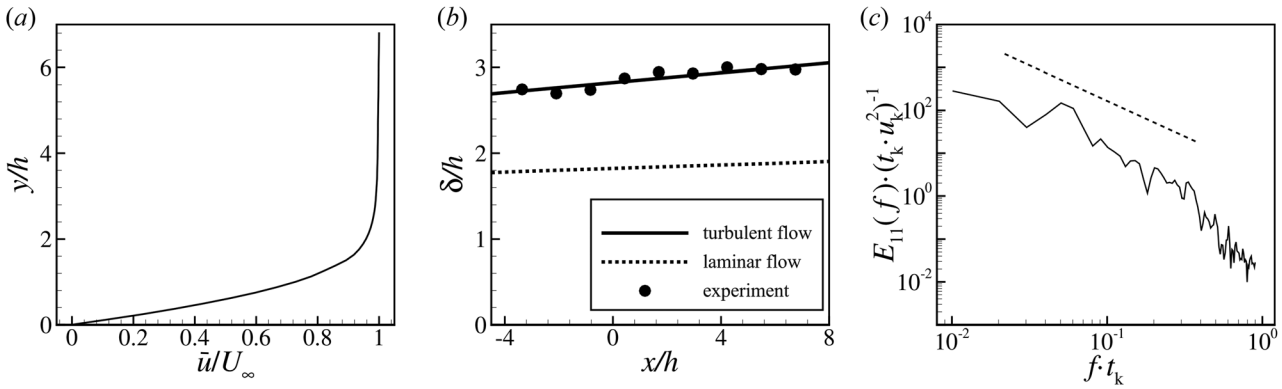

Fig. 2 (*a*) The profile of ensemble average streamwise velocity $\bar{u}$ at x/h=0. (*b*) The development of the boundary layer thickness $\delta(x)$. (*c*) The spectra of the streamwise fluctuation velocity $E_{11}(f)$ at the point $(x/h, y/h)=(0, 1.4)$, where the dashline marks a −5/3 scaling.

underestimated moderately according to Ref. [18]. The height of the rod array is $h = 3$ mm (see Fig. 1(*e*)), so that the rods are approximately submerged in the boundary layer (see Figs. 3(*a*) and 3(*c*)). The distance between the leading edge of the rod array to the leading edge of airfoil in the supporter is 150 mm. The rod-rod interval is $s = 10$ mm (see Fig. 1(*e*)), giving the relative interval of $s/d = 2$ (and the open-area ratio of $(s-d)/d = 1$), slightly different to 3–4 (0.66–0.75) in Ref. [10].

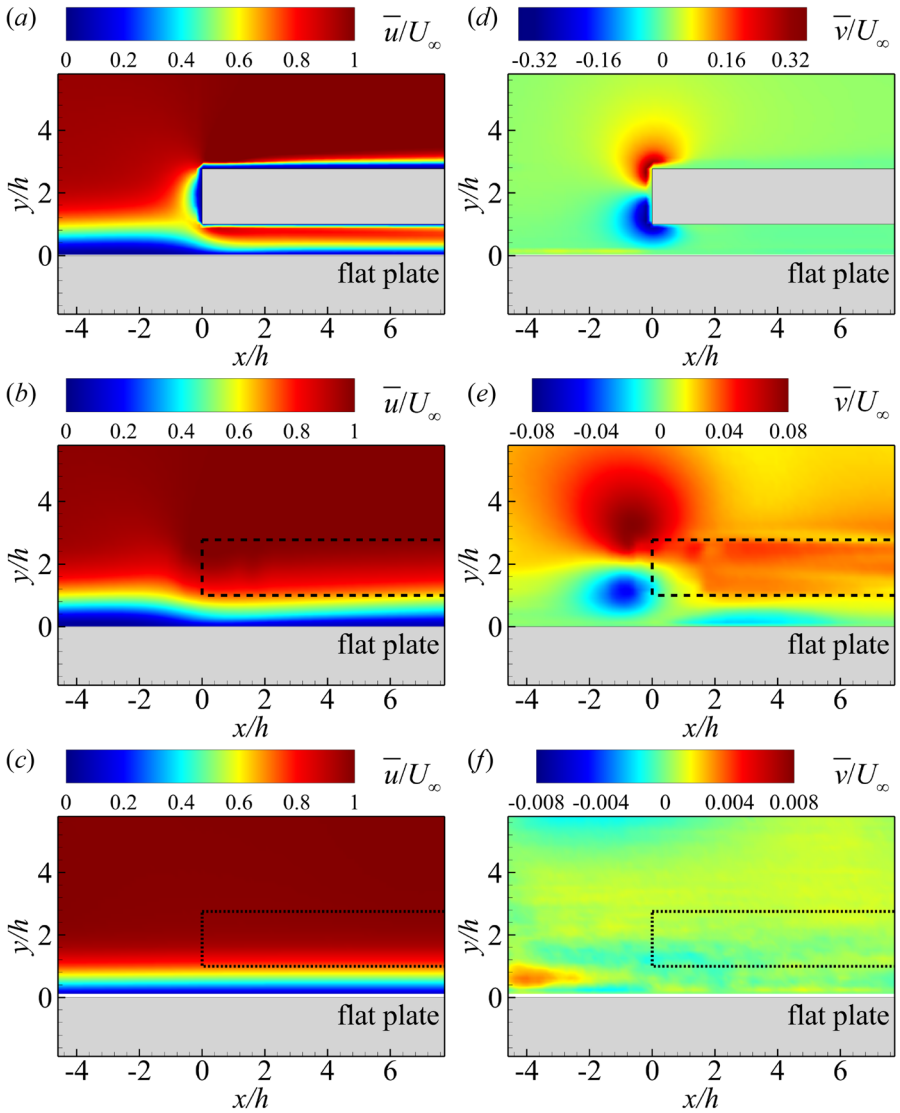

Fig. 3 Contours of the mean streamwise velocity $\bar{u}$ (*a*)–(*c*) and the mean normal velocity $\bar{v}$ (*d*)–(*f*) in the planes of z/h=0 (*a*, *d*) and –1.67 ($z/s=-0.5$) ((*b*) and (*e*)), the dash line marks the rod position for reference) for the experiment group and the counterpart group ((*c*) and (*f*)), the dot line marks the rod position for reference)

Particle image velocimetry Measurement. Two-dimensional PIV measurements were carried out in this study. The fluorescent PIV tracers in diameter of about 2 μm were seeded in the NaI solution in the water tunnel. A dual-head pulse laser (Beamtech Vlite-Hi-527) was used to generate a light sheet through a group of lenses and mirrors. A high-speed camera (Phantom) was used to take the PIV images. The sampling rate of the measurement is 1000 Hz. The inter-rogation window of 48 pixels was used and followed by window size reducing to a final window size of 24 pixels (50% overlap) [19], and the neighboring vector spacing is approximately 0.38 mm in this study.

A Cartesian coordinate was set, as sketched in Figs. 1(*d*) and 1(*e*). The X axis denotes the flow streamwise direction, and the Y axis points to the wall normal direction. The Z axis shows the spanwise direction. The projection of leading edge of the center rod on the top surface of the flat plate is defined as the origin of the coordinate. The measurements were taken in two groups. One is with the rod array as the experiment group, while another is the case without the rod array but keeping the flat plane and the rod supporter as the counterpart group. The measurements were carried out at two XY planes, $z/h = -1.67, 0$, and three XZ planes, $y/h = 0.68, 1.8, 3.15$, as summarized in Table 1. Given that the spatial resolution and field-of-view of the measurements are determined by the maximum number of pixels of the camera sensor [20], the camera was adjusted by balancing the consideration of the measurement domain (for obtaining large flow structures) and pixel resolution for resolving small flow structures between the rod array and the plate. For each measurement plane in each group, 10000 instantaneous samples were measured and taken into the statistics.

Pressure Calculation. With the calculated instantaneous velocity from PIV, the instantaneous pressure distribution was solved by the Poisson equation method, based on the assumption that the three dimensional effect was weak to be negligible. The three-dimensional form of the pressure Poisson equation in XY plane (derived from Navier–Stokes equations) is

$$\begin{aligned}\frac{\partial^2 p}{\partial x^2}+\frac{\partial^2 p}{\partial y^2} &= -\rho\left\{\left(\frac{\partial u}{\partial x}\right)^2+2\frac{\partial v}{\partial x}\frac{\partial u}{\partial y}+\left(\frac{\partial v}{\partial y}\right)^2\right\}\\ &-\rho\left\{\frac{\partial \mathrm{div}_{xy}}{\partial t}+u\frac{\partial \mathrm{div}_{xy}}{\partial x}+v\frac{\partial \mathrm{div}_{xy}}{\partial y}\right\}\\ &+\mu\left\{\frac{\partial^2 \mathrm{div}_{xy}}{\partial x^2}+\frac{\partial^2 \mathrm{div}_{xy}}{\partial y^2}\right\}\\ &\boxed{-\rho\left\{\frac{\partial w}{\partial x}\frac{\partial u}{\partial z}+\frac{\partial w}{\partial y}\frac{\partial v}{\partial z}+w\frac{\partial \mathrm{div}_{xy}}{\partial z}\right\}+\mu\frac{\partial^2 \mathrm{div}_{xy}}{\partial z^2}}\end{aligned} \tag{1}$$

with the boundary conditions of

$$\begin{aligned}\frac{\partial p}{\partial x} &= -\rho\left\{\frac{\partial u}{\partial t}+u\frac{\partial u}{\partial x}+v\frac{\partial u}{\partial y}\right\}+\mu\left\{\frac{\partial^2 u}{\partial x^2}+\frac{\partial^2 u}{\partial y^2}\right\}\\ &\boxed{+\left\{-\rho w\frac{\partial u}{\partial z}+\mu\frac{\partial^2 u}{\partial z^2}\right\},}\\ \frac{\partial p}{\partial y} &= -\rho\left\{\frac{\partial u}{\partial t}+u\frac{\partial v}{\partial x}+v\frac{\partial v}{\partial y}\right\}+\mu\left\{\frac{\partial^2 v}{\partial x^2}+\frac{\partial^2 v}{\partial y^2}\right\}\\ &\boxed{+\left\{-\rho w\frac{\partial v}{\partial z}+\mu\frac{\partial^2 v}{\partial z^2}\right\}}\end{aligned} \tag{2}$$

in which $\mathrm{div}_{xy} = \partial u/\partial x + \partial v/\partial y$.

Table 1 Dimensions of the measurement field-of-view

	x/h	y/h	z/h
XY plane	$-5 \sim 8$	$-2 \sim 6$	$-1.67, 0$
XZ plane	$-6 \sim 10$	0.68, 1.8, 3.15	$-5 \sim 5$

The boxed components in Eqs. (1) and (2) are unavailable in the two-dimensional PIV measurements, thus not included in calculation of pressure. The uncertainty of the pressure is estimated (see Appendix). Details of the Poisson method can be found in Refs. [21,22]. In the numerical implementation of the Poisson equation method in this study, the second-order central differentiation was applied for the discretized derivation in space and time, so that the pressure at the boundaries is one layer of grid inward of the velocity domain. The Neumann boundary condition, $\partial p/\partial x$ and $\partial p/\partial y$ obtained by the velocity data according to Eq. (2), was applied to boundaries of the domain. The pressure at the top left point in the domain was taken as the reference pressure. The matrix version of the Poisson equation was solved by a noniterative method through taking the inverse of the linear operator in the equation.

Results

Velocity Results. The velocity results are shown in this section for the XY planes and XZ planes, respectively. The velocity and lengthscale are nondimensionalized by the freestream velocity U_∞ and h for the y and z direction.

XY Planes. The ensemble averaged velocity $\bar{u}$ and $\bar{v}$, calculated by $\bar{(\cdot)} = (1/N)\sum_{j=1}^{N}(\cdot)_j$ (where j indicates the quantity at time j and N is the total number of samples), are shown in Fig. 3. The streamwise flow around the leading front of the rod can be seen in Figs. 3(*a*) and 3(*d*), from both of $\bar{u}$ and $\bar{v}$. The stagnation point is approximately at the center of the leading front of the rod (seen from panel *a* and *d*), and this indicates the quality of the alignment of the rod array and the respective measurements. From the leading front of the rod (i.e., $x/h = 0$), the boundary layer re-forms with the thickness growing on both the up and the bottom surface of the rod. The growth of the boundary layer above the rod is visually more rapidly than that at the flat plate, whereas the boundary layer at $z/h = -1.67$ ($z/s = -0.5$) at the flat plate grows visually rapidly. This leads to an expectation of undulant thickness of boundary layer at the flat plate along the spanwise direction at a fixed streamwise location. The existence of the rod also affects the flow for $x/h < 0$ that the boundary layer gets thicker than that of the counterpart (see Fig. 3(*c*)).

In the plane between the two neighboring rods, $z/h = -1.67$ ($z/s = -0.5$), the upward vertical flow can be seen in Fig. 3(*e*), in comparison the nearly vanished vertical flow in the counterpart group as shown in Fig. 3(*f*). This upward motion (for $x/h > 1, 1 \lesssim y/h \lesssim 3$) is still trivial, 5% of the streamwise velocity. For $x/h > 0$ and $y/h < 1$, small and noticeable downward vertical flow can be observed that the boundary layer is suppressed, in agreement with the re-formation of the boundary layer indicated by the streamwise velocity.

Large vorticity is attached to the top surface of the flat plate in the counterpart group (see Fig. 4(*c*)). Differently, the vorticity is attenuated close to the surface of the plate at $z/h = 0$ (see Fig. 4(*a*)) and starts to grow along the streamwise direction from $x/h = 0$, while the positive and the negative vorticity can be seen below and above the rod, respectively. In the plane of $z/h = -1.67$ ($z/s = -0.5$), the vorticity for $x/h < -1$ is slightly lifted up away from the plate and is increased in magnitude along the streamwise direction close to the plate.

We then examined the turbulent kinetic energy. Given by the two-dimensional measurements, the turbulent kinetic energy is estimated by the two measured velocity components, i.e., $k \approx (u'^2 + v'^2)/2$ as a surrogate, where $(\cdot)' = (\cdot) - \bar{(\cdot)}$ denotes the fluctuation of a quantity. As shown in Fig. 5, in reference to the counterpart group, the turbulent kinetic energy in the experiment group is increased at the upstream of the rod, for $0.4 \le y/h \le 1.6$. In addition, the turbulent kinetic energy is increased above and below the rod along the streamwise direction, resulted from the flow around the leading front of the rod. Below the rods, for both $z/h = 0$ and –1.67, the turbulent kinetic energy is reduced, while the location of

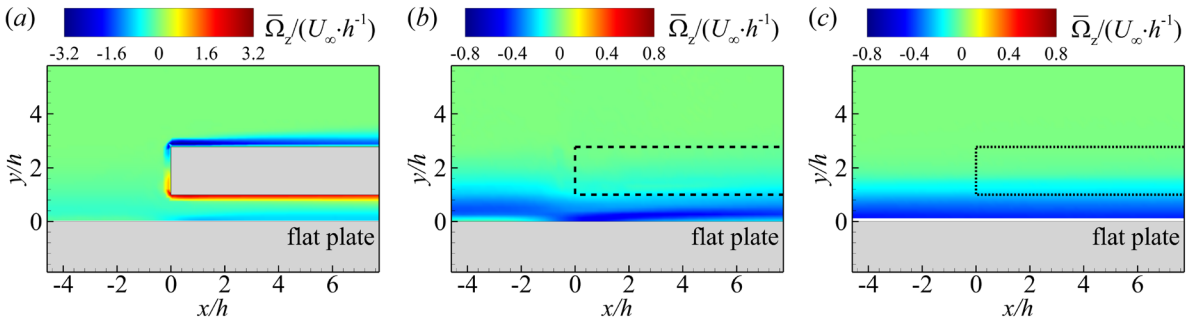

Fig. 4 Contours of the mean vorticity field $\bar{\Omega}_z$ in the planes of (*a*) $z/h = 0$ and (*b*) –1.67 ($z/s = -0.5$) (the dash line marks the rod position for reference) for the experiment group and (*c*) the counterpart group, where the dot line marks the rod position for reference

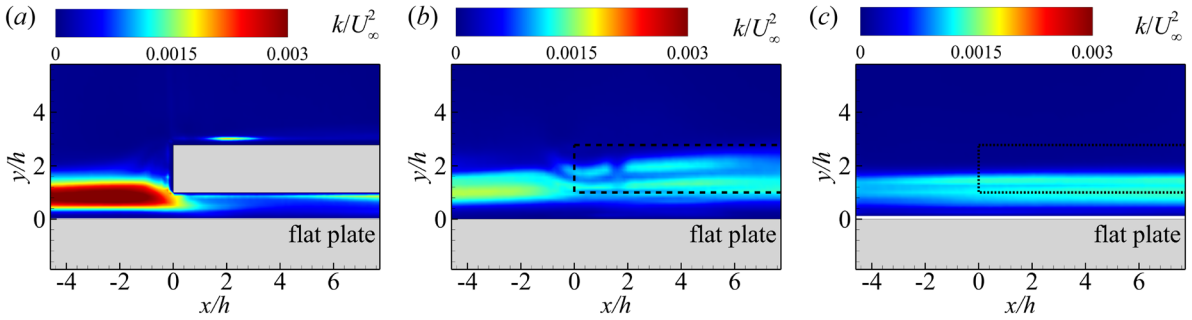

Fig. 5 Contours of the turbulent kinetic energy *k* in the planes of $z/h = 0$ (*a*) and –1.67 ($z/s = -0.5$) (the dashed line marks the rod position for reference) (*b*) for the experiment group and the counterpart group (*c*), where the dot line marks the rod position for reference

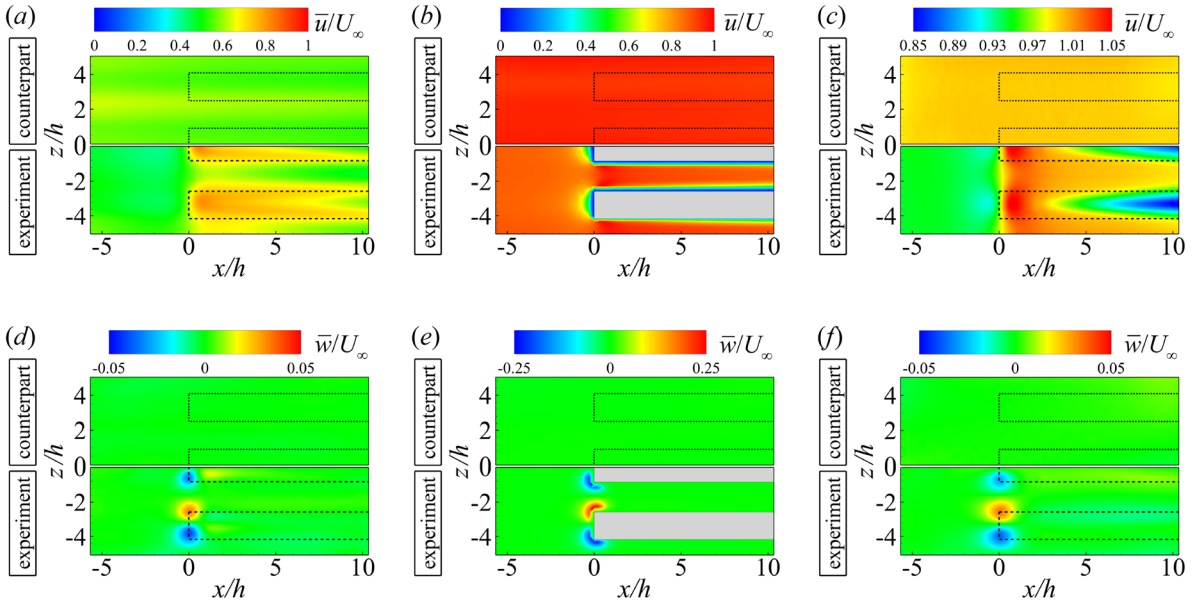

Fig. 6 Contours of the mean streamwise velocity $\bar{u}$ ((*a*)–(*c*)) and spanwise velocity $\bar{w}$ ((*d*)–(*f*)), in which the experiment groups lie in the lower halves and the counterpart groups in the upper halves, in the planes of $y/h = 0.68$ ((*a*), (*d*)), 1.8 ((*b*), (*e*)), and 3.15 ((*c*), (*f*)). The dashed line and dotted line mark the rod position for reference, respectively.

the noticeable turbulent kinetic energy is found to lift up slightly away from the plate, in reference to the counterpart group.

XZ Planes. The velocity results measured at the three *XZ* planes are shown in Fig. 6, where the results from the experiment and counterpart group are plotted side by side (and for figures in the rest of this section), for easy comparison. At the plane $y/h = 0.68$, for the experiment group, the streamwise stripes can be seen below the rods, especially close to $x/h = 0$ (see panel a). For the plane $y/h = 1.8$, between the rods, the streamwise velocity is increased from $\bar{u}/U_\infty \approx 0.8$ at $x/h = 0$ to $\bar{u}/U_\infty \approx 1$ at $x/h = 1$ and slowly decays back to $\bar{u}/U_\infty \approx 0.8$ around $x/h \approx 10$, for the z/h between

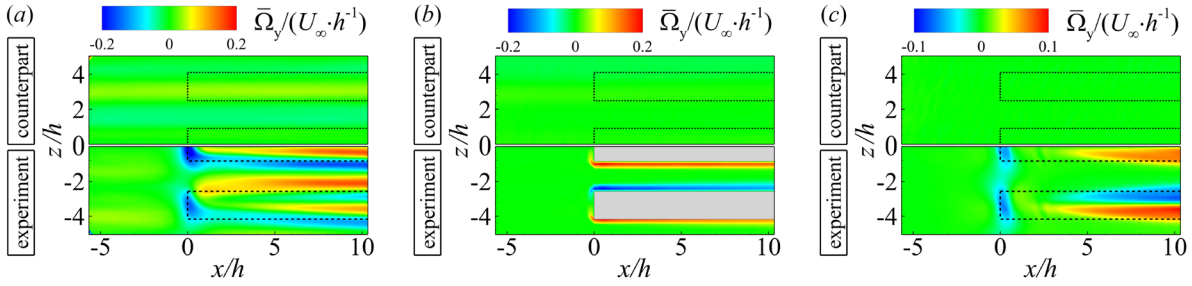

Fig. 7 Contours of the mean vorticity $\bar{\Omega}_y$, in which the experiment groups lie in the lower halves and the counterpart groups in the upper halves, in the planes of $y/h = 0.68$ (*a*), 1.8 (*b*), and 3.15 (*c*). The dashed line and dotted line mark the rod position for reference, respectively.

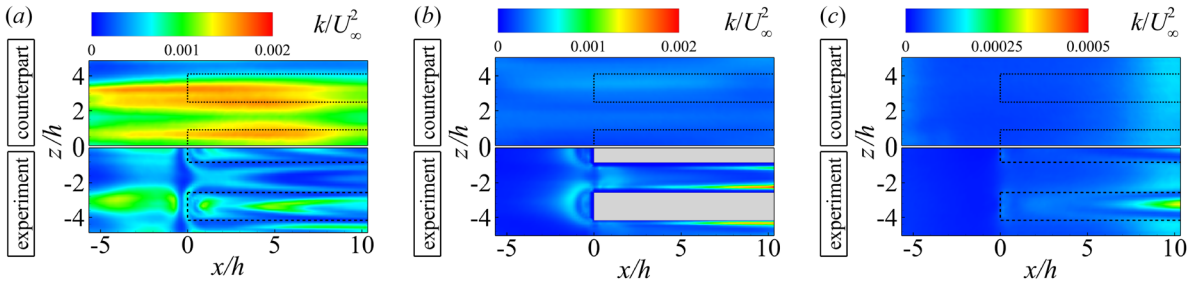

Fig. 8 Contours of the turbulent kinetic energy *k*, in which the experiment groups lie in the lower halves and the counterpart groups in the upper halves, in the planes of $y/h = 0.68$ (*a*), 1.8 (*b*), and 3.15 (*c*). The dash line and dot line mark the rod position for reference, respectively.

two neighboring rods, while the re-formation of the boundary layers at the rod surfaces can be seen with the nearly linear increase of the boundary layer thickness.

For the measurement plane above the rods, $y/h = 3.15$, the fast increase of the streamwise velocity can be observed at $x/h \approx 0$. Then, the streamwise velocity is decreased to $\bar{u}/U_\infty \approx 0.95$ at $x/h \approx 5$ and further decreased to $\bar{u}/U_\infty \approx 0.85$ (smaller than the flow speed $x/h < 0$ and also that in the counterpart group) at $x/h \approx 10$. As expected, the mean spanwise velocity is nearly zero in the counterpart group for the three measurement planes (see Fig. 6). In the experiment group, spanwise flow around the leading front of the rods is $\bar{w}/U_\infty \approx 0.05$ in the plane close to the flat plate ($y/h = 0.68$), $\bar{w}/U_\infty \approx 0.25$ in the plane crossing the array of the rods ($y/h = 1.8$), and $\bar{w}/U_\infty \approx 0.04$ in the plane above the rods ($y/h = 3.15$). In addition, weak stripes along the streamwise direction can be seen.

The stripes along the streamwise direction can be also seen in the vorticity field $\bar{\Omega}_y$ in the experiment group, in comparison to the counterpart group, as shown in Fig. 7. Around the leading fronts for the rods, the noticeable vorticity can be observed from all three measurement planes.

We then examined the turbulent kinetic energy in the experiment group. The increase of the turbulent kinetic energy at the upstream of the leading front of the rods can be seen in Fig. 8, at the plane of $y/h = 0.68$ and $y/h = 1.8$, in consistent with the observation in the XY plane. In the former plane, the turbulent kinetic energy seems to be slightly smaller than that in the counterpart group for $x/h > 0$. This suggests the shielding of the turbulence, as pointed out in the RANS simulations with the $k - \epsilon$ model in Ref. [10]. In the plane of $y/h = 3.15$, the increase of the turbulent kinetic energy can be only noticed at downstream locations, possibly resulted from the unsteady vortices shed from the leading fronts of the rods.

Pressure. The pressure field is obtained through the Poisson equation method, with a pressure reference point set at $(x/h, y/h) = (-5, 6)$ (the top left corner of the measurement field-of-view) in the *XY* plane. This point locates at the freestream and most upstream in the measurement field-of-view, and the pressure at this point is assumed to be approximately constant in time, as suggested by the nearly zero of the turbulent kinetic energy (see Fig. 5). Similar choice of the reference pressure was also used in a cavity flow, where the pressure at the freestream above the square cavity was assumed to be constant and taken as the reference point [22].

Given that at the plane $z/h = 0$, the pressure field was separated by the rod into three parts, and this is beyond the capability of our pressure-Poisson solver. Thus, in this Section, the pressure at the plane $z/h = -1.67$ ($z/s = -0.5$) is shown for the experiment group while for the plane $z/h = 0$ of counterpart group (where data at $z/h = 0$ and $z/h = -1.67$ are the same given by the fact that flow is independent spanwisely). In the closely referred study of Ref. [10], the pressure was not mentioned in the plane between two neighboring rods (the $z/s = -0.5$ plane). Our measurement of the pressure in this plane gives the missing part in their study, and can be compared with their RANS simulation results shown for this plane.

The ensemble averaged pressure field $\overline{P - P_\infty}$ in the XY plane is shown in Fig. 9. For the experiment group, the pressure first increases along the streamwise direction, reaching the global maximum of the field-of-view at $x/h \approx -1.6$, $y/h \approx 2$, then decreases to the global minimum at $x/h \approx -1.6$, $y/h \approx 2$, and increases to an approximate constant from $x/h \approx 4$ to the end of the field-of-view. The most significant change of pressure, i.e., the direction of maximum gradient direction is approximately parallel to the x axis at the level of $y/h \approx 2$, which is the same level of the vertical center of the rod array. The local change of the pressure in the experiment group is possibly due to the flow around the leading front of the rod, in approximate agreement with streamwise range of the velocity change (see Fig. 3). In the counterpart group, the pressure remains approximately constant compared to the level of the pressure change in experiment group.

The time series of the pressure at three streamwise points close to the plate surface ($y/h = 0.25$) and three streamwise points slightly above the rod ($y/h = 3.15$) is extracted to calculate the sound pressure level (SPL). The SPL was calculated by

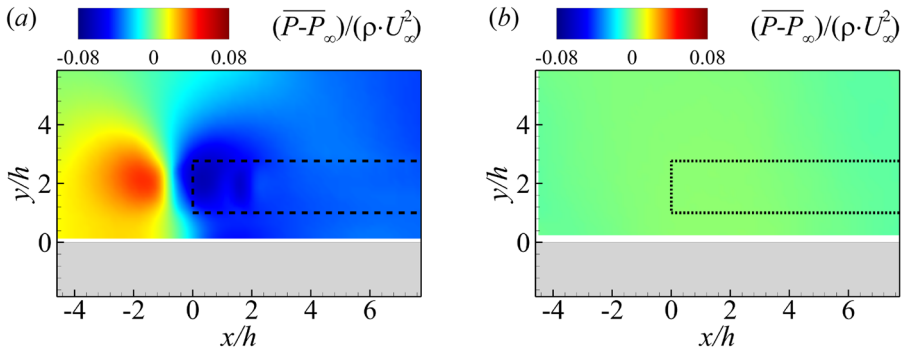

Fig. 9 Contours of the mean pressure $\overline{P-P_\infty}$ in the planes of $z/h=-1.67$ ($z/s=-0.5$) for the experiment group (*a*) (where the dashed line marks the rod position for reference) and the counterpart group (*b*) (where the dotted line marks the rod position for reference)

$$\mathrm{SPL} = 10\log_{10}(G_{\mathrm{PP}}/P_{\mathrm{ref}}^2) \tag{3}$$

where G_{PP} is the one-sided pressure power spectral density [10], and in this study the reference power spectral density $P_{\mathrm{ref}} = 1\mu\mathrm{Pa}/\sqrt{\mathrm{Hz}}$ as commonly used in liquid flow [23]. To calculate G_{PP}, the ensemble average of the pressure is removed, before the application of Welch method with 50% overlapped Hamming window in length of 1000 temporal sample points. The sound pressure levels are shown in Fig. 10. The very low frequency range of the curves is cut off, because of insufficient number of data points. The SPL curves generally increase to reach respective approximate plateaus before the sharp decrease. In theory, three scalings, 2, –1, and –5 in power of frequency (as marked in Fig. 10), are expected for the low, middle, and high frequencies [24]. The SPL curves can roughly follow the three scalings for both the experiment and the counterpart group.

For all three position $x/h = 0$ (the leading front of the rod), $x/h = 4$, and 7.7, the SPL of the experiment group is lower than that of the counterpart group for the investigated range of frequencies. This scenario is expected to hold for further downstream locations, as learned from Ref. [10]. The slight difference of SPL between the position $y/h = 0.25$ and $y/h = 3.15$ is that for the latter the SPL seems follows a better scaling of 2 for the range of low frequencies, while for the former, the SPL seems follows a better scaling of –5 for the high frequencies in the experiment group.

To quantify the attenuation of the pressure fluctuations produced by the rod array, the attenuation of the sound pressure level is obtained by

$$\Delta\mathrm{SPL} = -10\log_{10}(G_{\mathrm{PP}}^{\mathrm{experiment}}/G_{\mathrm{PP}}^{\mathrm{counterpart}}) \tag{4}$$

As shown in Fig. 11, ΔSPL is generally positive, giving the attenuation of the turbulence noise in this study, whereas negative ΔSPL indicates the increase of the noise. For $y/h = 0.25$, it can be seen that the noise reduction is decreased from $x/h = 0$ to $x/h = 4$, and then is increased from $x/h = 4$ to $x/h = 7.7$ (see Fig. 11(*a*)). This minimum of the noise reduction at $x/h = 4$ is possibly due to that the vortices shedding off the leading front of the rod interact with the boundary layer over the flat plate at this downstream location.

At $y/h = 3.15$, however, at leading edge $x/h = 0$, the noise is amplified given $\Delta\mathrm{SPL} < 0$, whereas the noise is found to be reduced

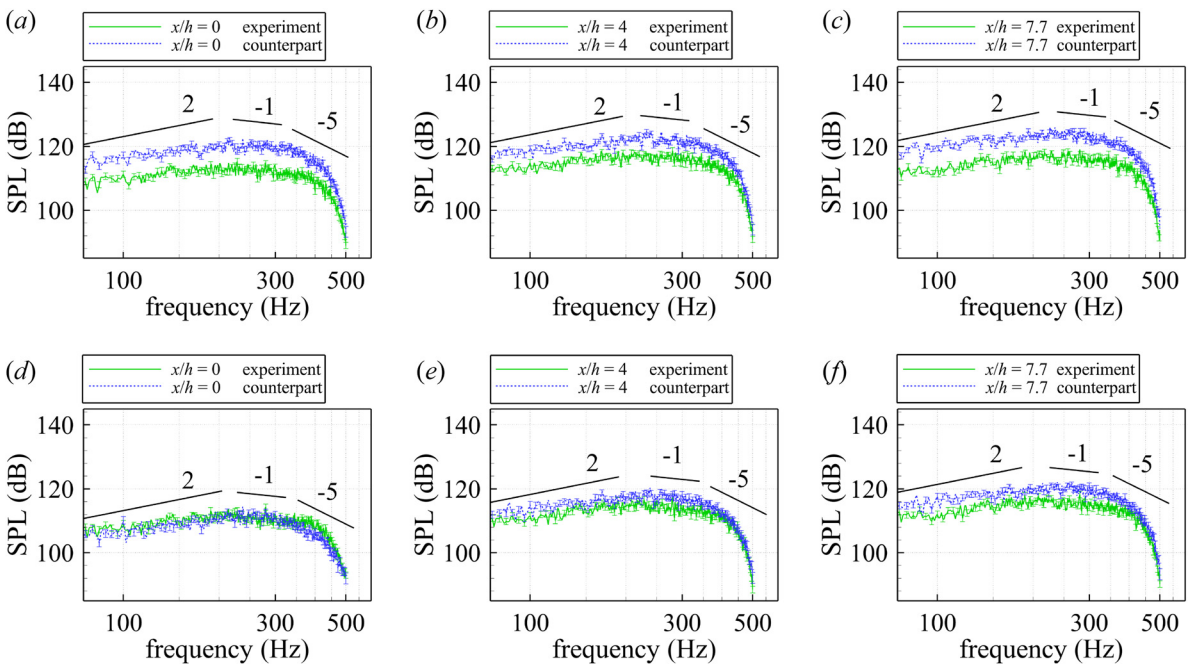

Fig. 10 The sound pressure level of the experiment group and the counterpart group close to the plate surface ($y/h = 0.25$, (*a*)–(*c*)) and slightly above the top surface of the rod ($y/h = 3.15$, (*d*)–(*f*)). The columns of the panels from left to right correspond to $x/h = 0$ ((*a*), (*d*)), 4 ((*b*), (*e*)) and 7.7 ((*c*), (*f*)), respectively.

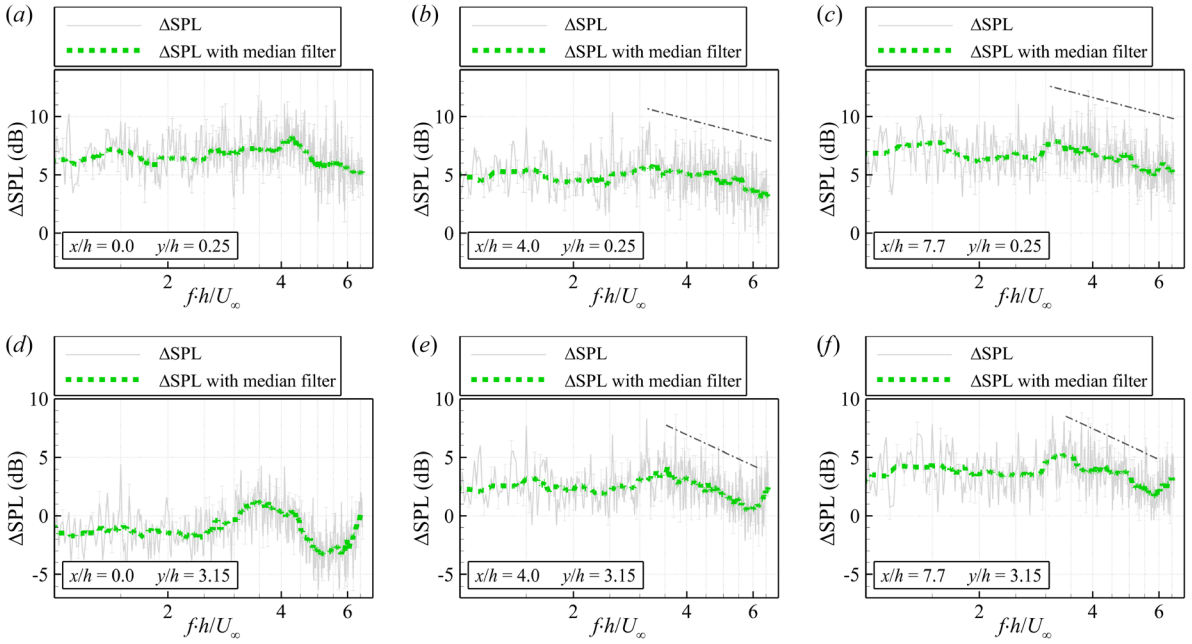

Fig. 11 The attenuation of the sound pressure level of the experiment group in reference to the counterpart group close to the plate surface ($y/h = 0.25$, (*a*)–(*c*)) and slightly above the top surface of the rod ($y/h = 3.15$, (*d*)–(*f*)). The dot lines denote the results obtained from of directly calculated ΔSPL in solid line.

in downstream at $x/h = 4, 7.7$ ($\Delta SPL > 0$). For the frequency $fh/U_\infty < 3$, ΔSPL maintains an approximately constant level for all the three streamwise locations. An interesting and noticeable trend can be seen for $3.5 < fh/U_\infty < 6$, as eye-guided by the dash line in (e–f). This scaling indicates approximately 16 dB decrease in ΔSPL over an order of magnitude of the dimensionless frequency, and this is larger than about 4 dB (in an order of magnitude of frequency) at further downstream locations in the study of Ref. [10] (see their Fig. 18). An increasing of the ΔSPL can be observed at the further larger dimensionless frequency, but it is difficult to be quantified due to the short range of this trend, limited by the sampling frequency in this study. Similar observation can be also found at $y/h = 0.25$, except that at $x/h = 0$ the noise reduction can be clearly seen. For $fh/U_\infty > 3$, a decreasing trend in a scaling that ΔSPL drops about 8 dB over an order of magnitude of the dimensionless frequency can be approximately found, see the dot lines in (b)–(c), which are obtained from taking the median filtering operation for the data shown in solid lines.

To elucidate the pressure noise attenuation, we examine the profiles of $\partial\bar{u}/\partial y$ and that of the root-mean-square of the normal velocity fluctuation v' at $x/h = 7.7$. It is the very downstream location in the measurement domain that the effect of the flow around the leading front of rod is assumed to be trivial. According to the analysis in Ref. [25], the reduction of pressure fluctuations at the surface is attributed from the decrease of either the vertical velocity fluctuations, or the velocity shear close to the wall, or from their combination. As shown in Fig. 12, for $y/h \approx 0$ (close to the wall), the velocity shear quantified by velocity gradient $\partial\bar{u}/\partial y$ and the vertical velocity fluctuation quantified by the root-mean-square of v' are both decreased in the experiment group as compared with the counterpart. The decrease of these two quantities causes the attenuation of the pressure noise at $y/h = 0.25$ (see the purple curve in Fig. 11), as demonstrated in the model of Ref. [25] and generally supported by the analysis of Refs. [26,27] and theoretical work of Ref. [28].

Velocity Spectra. In order to understand the redistribution of the velocity fluctuations caused by the rod array along the spanwise direction, the two-dimensional spatial premultiplied power spectral density (PSD) of streamwise and spanwise fluctuating velocity was calculated at $y/h = 0.68$ and $y/h = 3.15$ in the XZ plane, with the data from $x/h = 0$ to $x/h = 10$. For both fluctuating velocity u' and w', one-sided PSD was obtained from two-dimensional fast Fourier transform (FFT) at each time instant, in which the velocity is normalized with U_∞ and weighted with Hanning window in both of streamwise and spanwise direction. The scaling factor applied in FFT is determined by the spatial sampling frequency, number of grid points in both dimensions and the window function, so that the integration of PSD gives the spatial variation of the velocity field. The wavenumber k_x and k_z are defined as the inverse of the wavelength in both dimensions corresponding to the PSD. With the PSD obtained at each time instant, the temporal average was performed and multiplied with the corresponding wavenumber in both dimensions. The premultiplied PSD for experiment group at $z/h = -1.67$ ($z/s = -0.5$) and counterpart group are presented in Figs. 13(*a*)–13(*h*), respectively.

At $y/h = 0.68$ (below the rod array), the rod array intensified both fluctuating velocity u' and w' in the experiment group in comparison to the counterpart group. The fluctuating velocity u' is enhanced in a wider range of length scales as shown in Figs. 13(*a*) versus 13(*e*), which could be observed from the expansion of the yellow contour level. However, compared to u', the enhancement of fluctuating velocity w' is observed in a narrower range of length scales, in the

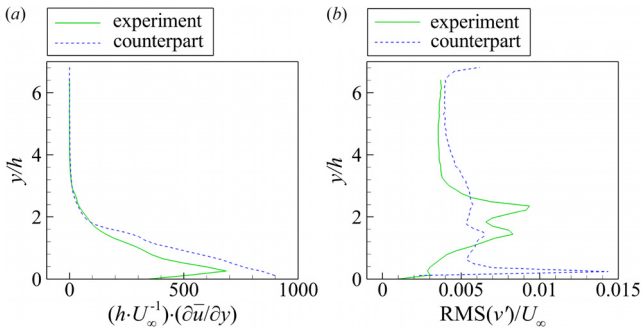

Fig. 12 (*a*) The profile of ensemble average velocity gradient $\partial\bar{u}/\partial y$ at $x/h = 7.7$. (*b*) The profile of the root-mean-square of the velocity fluctuation v' at $x/h = 7.7$.

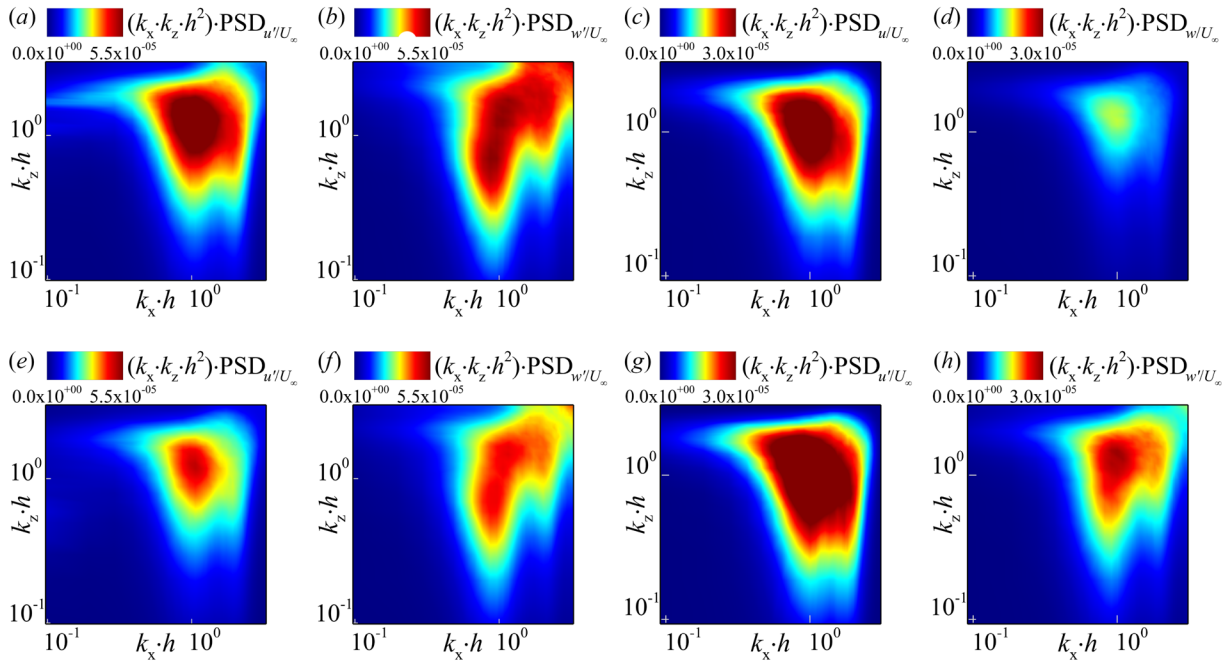

Fig. 13 Two dimensional spectra of the velocity fluctuations for the experiment group (*a*)–(*d*) and the counterpart group (*e*)–(*h*). The panel (*a*), (*b*), (*e*), (*f*) are from the data at $y/h = 0.68$, and the panel (*c*), (*d*), (*g*), (*h*) are from the data at $y/h = 3.15$. The panel (*a*), (*c*), (*e*), (*g*) and (*b*), (*d*), (*f*), (*h*) are from the velocity u' and w', respectively.

high wavenumber regime, see Figs. 13(*b*) and 13(*f*). This suggests that the rod array may bring more impact on fluctuating velocity in streamwise direction than in spanwise direction, which is possibly attributed to anisotropic flow structures, resulted from the shielding and suppressing effect of the canopy structures. Differently, at $y/h = 3.15$ (above the rod array), the rod array attenuated fluctuating velocity of the experiment group, i.e., u' and w', as shown in Figs. 13(*c*) versus 13(*g*), and 13(*d*) versus 13(*h*). The

Table 2 Parameters of the inspected modes in XZ planes

	frequency [Hz]		attenuation rate [s^{-1}]		amplitude [$m \cdot s^{-1}$]	
$y/h = 0.68$	experiment	counterpart	experiment	counterpart	experiment	counterpart
mode 1	9.5	10.6	−323.9	−42.5	2.4×10^{-2}	3.0×10^{-2}
mode 2	57.7	57.7	−393.5	−466.4	3.9×10^{-2}	2.8×10^{-2}
mode 3	406.1	406.0	−600.4	−657.5	9.3×10^{-3}	7.7×10^{-3}
	frequency [Hz]		attenuation rate [s^{-1}]		amplitude [$m \cdot s^{-1}$]	
$y/h = 3.15$	experiment	counterpart	experiment	counterpart	experiment	counterpart
mode 1	9.1	8.6	−28.2	−30.1	4.2×10^{-3}	1.0×10^{-1}
mode 2	89.2	88.4	−505.1	−651.3	1.5×10^{-2}	6.1×10^{-2}
mode 3	273.5	274.5	−606.6	−512.2	6.9×10^{-3}	1.0×10^{-2}
mode 4	443.1	443.5	−239.1	−305.0	1.5×10^{-2}	3.6×10^{-2}

Table 3 Parameters of the inspected modes in XY planes

	frequency [Hz]		attenuation rate [s^{-1}]		amplitude [$m \cdot s^{-1}$]	
$z/h = 0$	experiment	counterpart	experiment	counterpart	experiment	counterpart
mode 1	11.0	9.4	-54.1	-30.7	1.6×10^{-2}	2.0×10^{-2}
mode 2	139.4	138.0	-689.8	-459.3	1.5×10^{-3}	1.7×10^{-2}
mode 3	442.9	406.0	-790.5	-610.6	2.3×10^{-2}	8.3×10^{-3}
	frequency [Hz]		attenuation rate [s^{-1}]		amplitude [$m \cdot s^{-1}$]	
$z/h = -1.67$	experiment	counterpart	experiment	counterpart	experiment	counterpart
mode 1	12.4	9.4	-29.1	-30.7	6.2×10^{-3}	2.0×10^{-2}
mode 2	137.3	138.0	-610.6	-459.3	2.1×10^{-2}	1.7×10^{-2}
mode 3	441.5	441.6	-607.6	-610.6	4.5×10^{-3}	8.3×10^{-3}

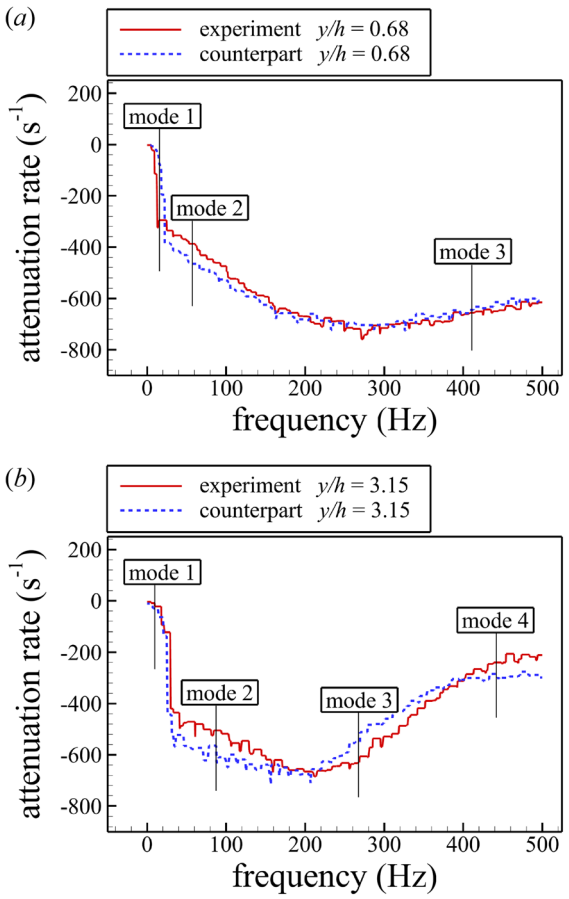

Fig. 14 The top envelope of the modes for the one-side attenuation rate of the cases in the XZ planes at y/h=0.68 (*a*) and y/h=3.15 (*b*). The mode 1–3 in (*a*) and the mode 1–4 in (*b*) are typical modes in the frequency regime.

attenuation is observed in a wider range of wavenumber of w' than u', in contrast to those at $y/h = 0.68$. The greater impact to spanwise fluctuating velocity than the streamwise one is possibly given by the vertical interaction of the freestream flow and the boundary layer

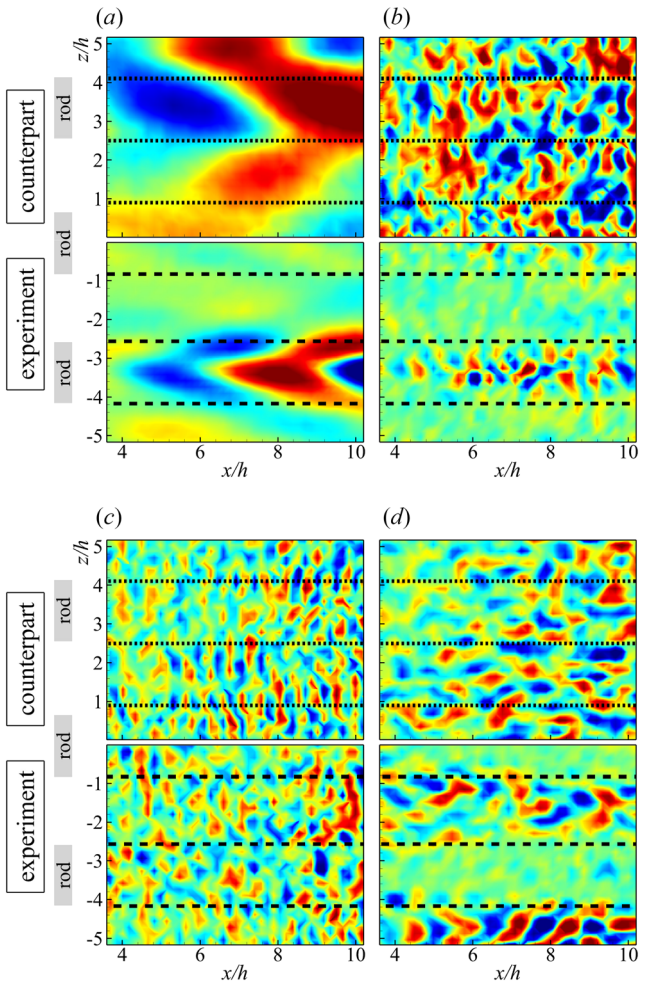

Fig. 16 Contours of the velocity corresponding to the mode 1–4 (*a*)–(*d*) in *XZ* planes at the level $y/h = 3.15$, as indicated in Fig. 14(*b*). The data of the experiment group and the counterpart group are shown half-half for easy comparison. The dot and dash lines as well as the 'rod' label on the left mark the rod position for reference.

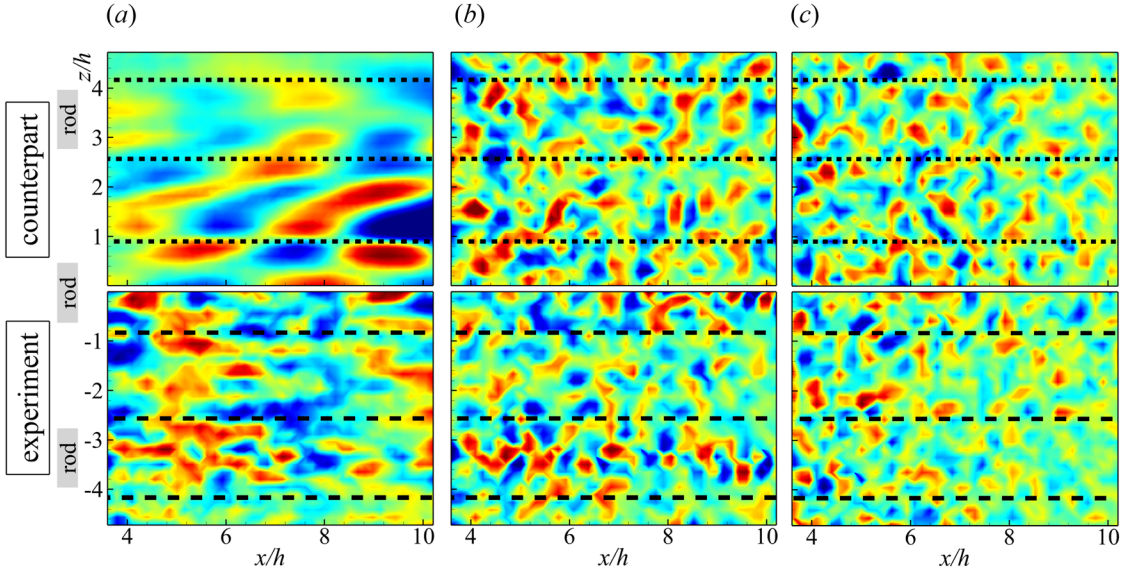

Fig. 15 Contours of the velocity field corresponding to the mode 1–3 (*a*)–(*c*) in the XZ plane at $y/h = 0.68$, as indicated in Fig. 14(*a*). The data of the experiment group and the counterpart group are shown half-half for easy comparison. The dotted and dashed lines as well as the "rod" label on the left mark the rod position for reference.

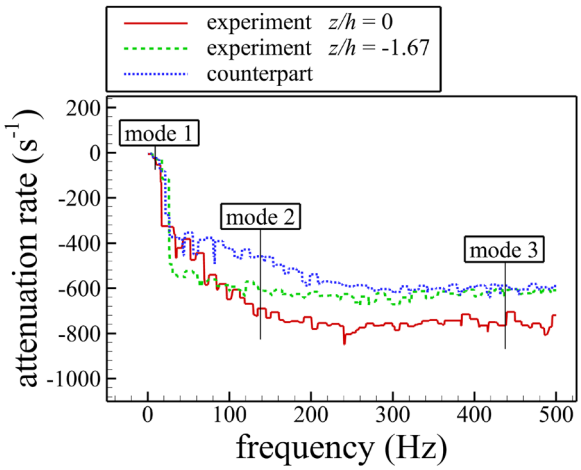

Fig. 17 The top envelope of the modes for the one-side attenuation rate of the cases in the XY planes, in which experiment group at $z/h = 0$ (solid line), $z/h = -1.67$ (dash line) and counterpart group (dot line). The mode 1–3 are typical modes in the frequency regime.

flow. The details of flow structures are rather three dimensional and need to be examined by three-dimensional velocity measurements (in a follow-up study). The reduction of the velocity fluctuations in both direction possibly implies the reduction of the vertical velocity fluctuations at $y/h = 0.68$, in agreement to the observation of the shielding effect of turbulence below the rod array [10], while falls into the theoretical framework of the pressure noise reduction in [25–28]. The increase of the velocity fluctuations at $y/h = 3.15$ requires further investigation to elucidate its potential mechanism link to the changes of sound pressure level (see Figs. 11(*d*)–11(*f*)), given that overall the canopy array gives the noise reduction in the far field [9].

Dynamic Mode Decomposition. In order to gain further insights into the spatio-temporally correlated flow patterns [29] and their changes resulted from the rod array, dynamic mode decomposition (DMD) was applied to the velocity fields at $y/h = 0.68$ and 3.15 as well as at $z/h = 0$ and –1.67. The streamwise range of the velocity data under consideration is $4 \lesssim x/h \lesssim 10$ for investigating the flow structures around the rod array, which are expected to share common characteristics. The flows around the leading edge are not under consideration because they are rather local and limited in a small streamwise region in practical applications (whose streamwise length is usually very large). To focus on the fluctuation velocity fields that are closely relevant to the noise, the ensemble averaged velocity is subtracted from the instantaneous velocity before applying the DMD analysis. The DMD of the velocity $(u', v')(t)$ is

$$(u', v')(t) \approx \sum_{k=1}^{N} (\tilde{u}, \tilde{v})_k \exp(\omega_k t)\, b_k \tag{5}$$

where $(\tilde{u}, \tilde{v})_k$ denotes the velocity (in the form of vector with unity norm) for the kth mode, ω_k and b_k are the corresponding complex frequency and initial amplitude for the kth mode, respectively. The real part of the complex ω_k denotes the attenuation rate and its imaginary part shows the frequency. N is the number of the total modes in this study (and sometime it is the number of modes after truncation due to computational unaffordability [30]). The details of the DMD can be found in Kutz et al. [30]. The detailed parameters of the featured DMD modes are summarized in Tables 2 and 3.

The attenuation rate of the cases as a function of the frequency from the XZ planes are shown in Fig. 14. Each line denotes the top envelope (upper bound) of the attenuation rate) of the respective mode points, which is obtained by connecting the largest attenuation rate from each of the small bin of the frequency. At $y/h = 0.68$ (the XZ plane below the rod array), the frequency range is separated into three regimes (by the cross points of the two lines), i.e., $0 - 20$ Hz, $20 - 160$ Hz and $160 - 500$ Hz. The corresponding typical modes are labeled as mode 1, 2, and 3, respectively, while their corresponding streamwise velocity fields are visualized in Fig. 15. For the mode 1 (with about 300 s^{-1} difference in attenuation rate), the experiment group has a lower attenuation rate which gives a smaller lifetime of the flow structures than the counterpart group. In the velocity contour (Fig. 15(*a*)) of the experiment group, the flow pattern covers $-4 < z/h < 0$ and $4 < x/h < 7$ (see the red and yellow area) blended with small flow structures, whereas the smooth tilted streamwise pattern, covering, e.g., $1 < z/h < 3$ and $4 < x/h < 8$, can be observed in the counterpart group. For the modes 2 and 3, the attenuation rate has smaller difference (i.e., about

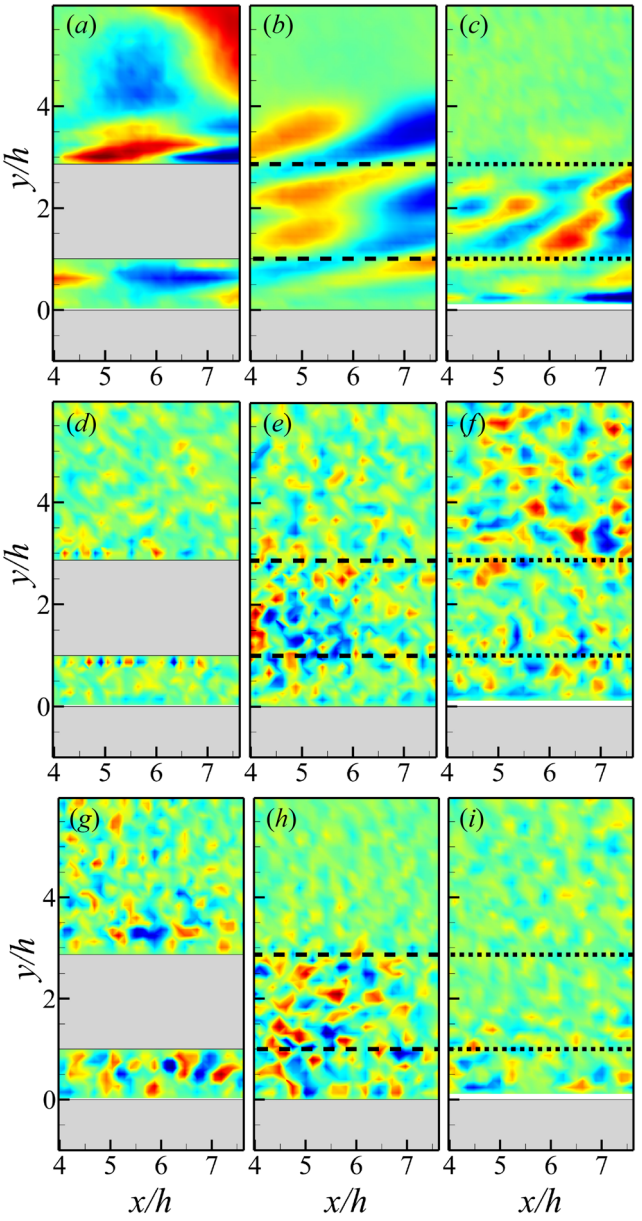

Fig. 18 Contours of the velocity field corresponding to the mode 1, 2, 3 (*a*)–(*c*), (*d*)–(*f*), (*g*)–(*i*) indicated in Fig. 17. The first column, (*a*), (*d*), (*g*), refers to the experiment group at z/h=0; the second column, (*b*), (*e*), (*h*), refers to the experiment group at z/h=−1.67, and the third column, (*c*), (*f*), (*i*), refers to the counterpart group. The dot and dash lines mark the rod position for reference.

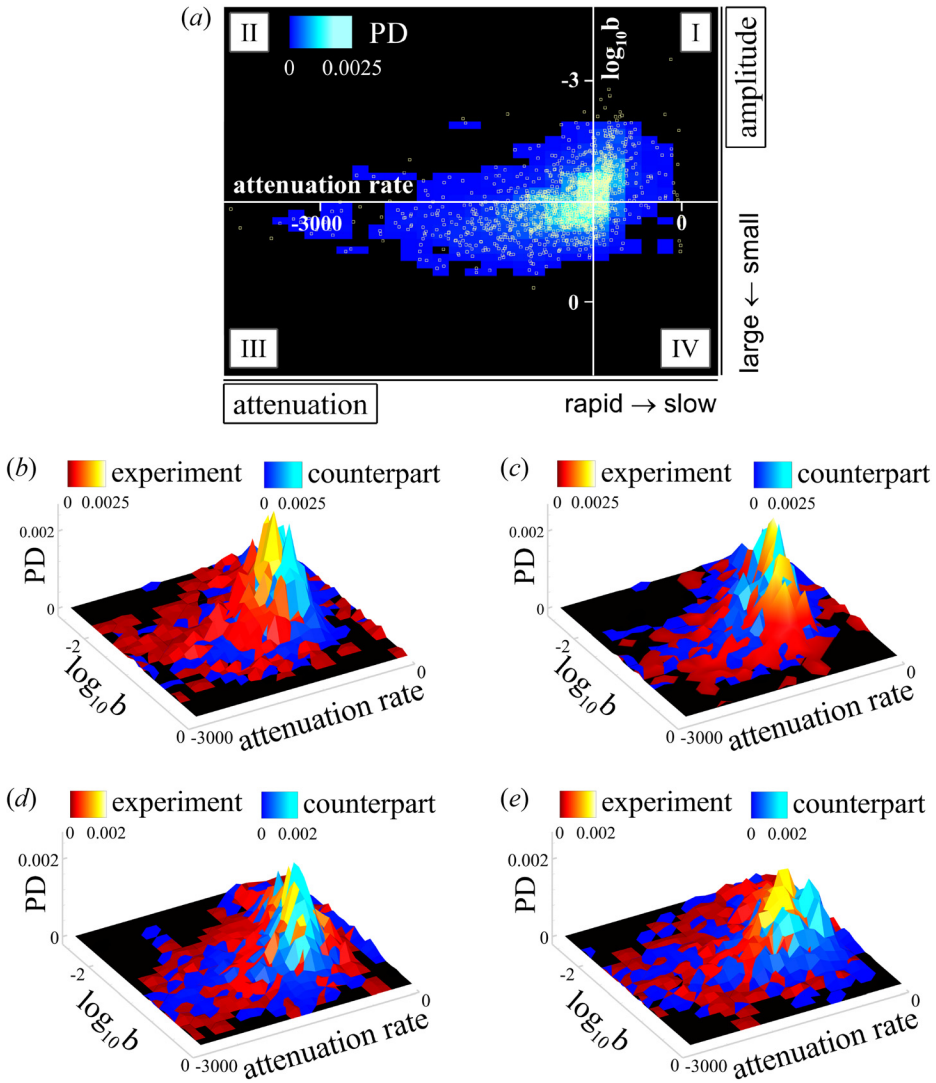

Fig. 19 Probability density distribution (PD) of the modes for the parameter space expanded by the attenuation rate and the amplitude of the respective modes. The modes of the counterpart group at the *XY* plane are displayed as hollow squares (*a*), while the probability density is shown in color. (*b*) and (*c*) denote the PD at $z/h = 0$ and $z/h = -1.67$, where the experiment group is shown in red–yellow mapping and the counterpart group in blue style. (*d*) and (*e*) denote the PD at $y/h = 0.68$ and $y/h = 3.15$, sharing the same color configuration as ((*b*)–(*c*)). In (*b*)–(*e*), *b* denotes the amplitude shown in logarithmic scale and the black level in contour shows PD $\approx$ 0.

100 and 40 s^{-1}) between the experiment and the counterpart group, and the difference in the respective velocity fields are also less noticeable (see Figs. 15(*b*) and 15(*c*)). Overall, the changes in flow pattern at this plane are approximately confined to low frequency (e.g., represented by the mode 1).

At $y/h = 3.15$ (the *XZ* plane over the rod array), four frequency ranges are obtained (i.e., 0 – 30 Hz, 30 – 210 Hz, 210 – 400 Hz, and 400 – 500 Hz), with typical modes labeled, while their streamwise velocity for the corresponding mode is shown in Fig. 16. For the mode 1, the experiment and the counterpart group have very similar attenuation rate. Small difference can be seen in velocity contour (Fig. 16(*a*)), where the streak pattern is approximately confined spanwisely above rod in the experiment group ($-4 < z/h < -2.5$), compared to the spanwisely widespread streak pattern in the counterpart group ($1 < z/h < 5$). Similar confinement of the flow patterns can also been seen for the mode 2 and 4, although the attenuation rates are clearly different between the two groups. Specifically, for the modes 2 and 4, the velocity pattern as local spots is observed in the experimental group, while the staggered larger pattern can be seen in the counterpart group.

Similar DMD examination was also carried out for the XY planes, as shown in Figs. 17 and 18. For the mode 1, streak patterns can be seen in Figs. 18(*a*)–18(*c*), where those in the counterpart (c) have more tilted angles, about $\pi/4$, and mostly locate for $1 < y/h < 3$. Differently, the streak flows in (a–b) have less tilted angles, and parts of them locate above the top plane of the rods ($y/h > 3$). For the modes 2 and 3, flow patterns in the experiment and the counterpart group are rather scattered, which differ mainly in their locating area. For both modes, the flow pattern at $z/h = -1.67$ for both the experiment and counterpart group are similar, see (e–f) and (h–i),

whereas their respect counterpart group are visually different that the scattered patterns are close to the wall (i) and away from from the wall (f).

Ranking the decomposed modes in either attenuation rate or amplitude of the modes may not fully demonstrate the characteristics of the flow field, given that sometime the attenuation rate and the energy are not exactly corresponded in the same order. Therefore, we consider the attenuation rate and the amplitude of the modes together in a statistical manner, through probability density distribution (*PD*) of the modes. In Fig. 19(*a*), as an example, the modes of counterpart in XY plane are labeled by yellow squares and the probability density is shown in contour. Centered at the peak of the distribution, four quadrants separate the distribution mapping. The *PD* is elongated along the quadrant I and III, the former of which corresponds to the flow structures with small amplitude and decay rate, while the latter indicates the flow in large amplitude but can rapidly decay. The quadrant II denotes the flow fluctuation in small amplitude and it can fast decay. The modes in the quadrant IV are least favored in noise reduction given that they refer that the flow pattern has large amplitude and decay slowly, whereas the quadrant II is most favored for the noise reduction. To better visualize the shift of the *PD* of the experiment group in reference to the counterpart group, the *PD* of the two groups are shown together in a three-dimension style, see Figs. 19(*b*)–19(*e*). No clear shift of the *PD* peak (and the distribution) can be observed in Figs. 19(*c*) and 19(*d*). Differently, distinct shift of the *PD* peak of the experiment group into the quadrant II can be observed in (b) and (e). Correspondingly, more modes in this quadrant are preferred for the noise reduction that the fluctuation flows turn to have small amplitude and can decay rapidly. Further examination of the characteristics of the flow patterns corresponding to these modes can give hints on alternative design of the pressure-shielding structures in a following study.

Conclusions

As a simplified prototype for recovering the features of owls' downy feathers, Clark et al. [9] and Gonzales et al. [10] experimentally found the sound pressure level is reduced by an array of strings/rods installed slightly above a flat plate. This is very valuable for the reduction of turbulence noise in practice. In this study, we took PIV measurements of the flow fields in a close analogical configuration of the pressure-shielding structures (i.e., rod array) as in Ref. [10], and attempted to shed lights into the change of the velocity fields by the rod array in the experiments.

Our experiments were carried out in a liquid tunnel, where the refractive index of the transparent solution is matched with that of the transparent experimental setup. The two-dimensional PIV measurements were taken at multiple planes to examine the flow characteristics. The turbulence fluctuations are found to be enhanced upstream of the leading front of the rods, particularly close to the surface of the plate. The existence of the rod array brings reformation of the boundary layer at the plate surface, in the meanwhile the turbulent kinetic energy is attenuated and the location of the noticeable turbulent kinetic energy is found to slightly lift away from the plate (in comparison to the counterpart group where the rod array is removed and only left with the rod supporter).

The velocity data were applied to obtain the pressure field, given the assumption that the missing velocity component in the Poisson method of solving the pressure field gives trivial influence to the pressure field. The temporal spectra of the pressure fluctuations show that the rod array attenuates the surface pressure fluctuations at $z/h = -1.67$ ($z/s = -0.5$) which was not examined and missed in the study of Ref. [10]. We also examined the changes of the characteristic flow patterns by the pressure-shielding structure through the dynamic mode decomposition. Clear changes of the flow pattern in certain modes by the canopy structures are observed. Further looking into these flow patterns can help improving design of the pressure-shielding in practice. In general, the findings of our study capture those in the referred study of Ref. [10]. In addition, this study has further provided velocity and pressure data in a high resolution manner for the plane between two neighboring planes, and particularly for the regions above the rod array, which is technically difficult to be obtained with pointwise velocity and pressure sensors (and avoid contaminating the flow fields in the meantime). This study demonstrates a technical possibility for investigating this interesting flow problem with careful PIV or PTV (particle tracking velocimetry) measurements. To better estimate the far-field noise with the rod array, the time-resolved high-resolution three-dimensional PIV [31,32] or PTV measurements, together with simultaneous recording of the pressure as reference, are required for the noise estimation in the framework of the acoustic analogy theories [33] in a future study.

Acknowledgment

The authors thank Professor Yiwei Wang for generously letting us use his experimental facility. The authors would like to thank Dr. Ting Wu for the fruitful discussion and physical insights into the turbulence noise and Dr. Hongping Wang for sharing of experience on the Poisson equation method. The authors also would like to thank anonymous reviewers for their valuable comments and suggestions, which improve the quality of this paper. Last but not least, the authors would like to express gratitude to Mr. Chenli Wang for his technical support throughout the experiments.

Funding Data

- National Natural Science Foundation of China (Award Nos. 11988102 and 92152106; Funder ID: 10.13039/501100001809).

Data Availability Statement

The datasets generated and supporting the findings of this article are obtainable from the corresponding author upon reasonable request.

Nomenclature

d = rod diameter
div_{xy} = velocity divergence in XY plane
G_{PP} = one-sided pressure power spectral density
h = rod array height
k = turbulent kinetic energy
k_x, k_z = wavenumber along x and z direction, respectively
L = distance between the leading edge of the flat plate and the leading front of the rod array
p = pressure
P_{ref} = reference power spectral density
$\overline{P - P_\infty}$ = mean pressure
PD = probability density
PSD = power spectral density
SPL = sound pressure level
s = rod-rod interval
t = time
U_∞ = mean streamwise freestream velocity
u, v, w = streamwise, vertical and spanwise velocity, respectively
$\bar{u}, \bar{v}, \bar{w}$ = streamwise, vertical and spanwise mean velocity, respectively
u', v', w' = streamwise, vertical and spanwise fluctuation velocity, respectively
x, y, z = coordinate system
ΔSPL = attenuation of sound pressure level
δ = boundary layer thickness
μ = dynamic viscosity
ν = kinematic viscosity
ρ = density
$\bar{\Omega}_y, \bar{\Omega}_z$ = mean vorticity along y and z direction, respectively

Appendix: Estimation of Uncertainty for Sound Pressure Level

The pressure Poisson equation in the XY plane, i.e., the Eq. (1), is repeated below for convenience.

$$\frac{\partial^2 p}{\partial x^2}+\frac{\partial^2 p}{\partial y^2}=-\rho\left\{\left(\frac{\partial u}{\partial x}\right)^2+2\frac{\partial v}{\partial x}\frac{\partial u}{\partial y}+\left(\frac{\partial v}{\partial y}\right)^2\right\}-\rho\left\{\frac{\partial \mathrm{div}_{xy}}{\partial t}+u\frac{\partial \mathrm{div}_{xy}}{\partial x}+v\frac{\partial \mathrm{div}_{xy}}{\partial y}\right\}+\mu\left\{\frac{\partial^2 \mathrm{div}_{xy}}{\partial x^2}+\frac{\partial^2 \mathrm{div}_{xy}}{\partial y^2}\right\}\boxed{-\rho\left\{\frac{\partial w}{\partial x}\frac{\partial u}{\partial z}+\frac{\partial w}{\partial y}\frac{\partial v}{\partial z}+w\frac{\partial \mathrm{div}_{xy}}{\partial z}\right\}+\mu\frac{\partial^2 \mathrm{div}_{xy}}{\partial z^2}}$$

where $\mathrm{div}_{xy}=\partial u/\partial x+\partial v/\partial y$.

Given by the two-dimensional measurements, the last two terms on the right hand size of Eq. (1) (as marked) cannot be obtained. To estimate the measurement uncertainty for pressure and the sound pressure level, the effect of the lacking terms on the uncertainty is taken into consideration by assuming the missing of the terms as additional noise. The truncated terms are estimated at a line $(y/h, z/h)=(0.68,-1.67)$ through the measurements in the XZ plane. In the meanwhile, the terms, i.e., $\rho u\partial \mathrm{div}_{xy}/\partial x$, $\rho v\partial \mathrm{div}_{xy}/\partial y$, $\mu\partial^2 \mathrm{div}_{xy}/\partial x^2$ and $\mu\partial^2 \mathrm{div}_{xy}/\partial y^2$ which share the similar forms as the corresponding truncated terms, are estimated at the same positions in the X-Y plane. Taking the statistics at the point $(x/h, y/h, z/h)=(7.7, 0.68, -1.67)$ as an example, the probability density function (PDF) of the terms is shown in Fig. 20. $\rho w\partial \mathrm{div}_{xy}/\partial z$ is found to lead the truncated terms in magnitude in terms of their standard deviation. Even so, it is about one tenth of the term $\rho u\partial \mathrm{div}_{xy}/\partial x$ in magnitude.

The truncated term $\rho(\partial w/\partial y)(\partial v/\partial z)$ cannot be estimated using the current data and is assumed to be small than the dominant term in magnitude.

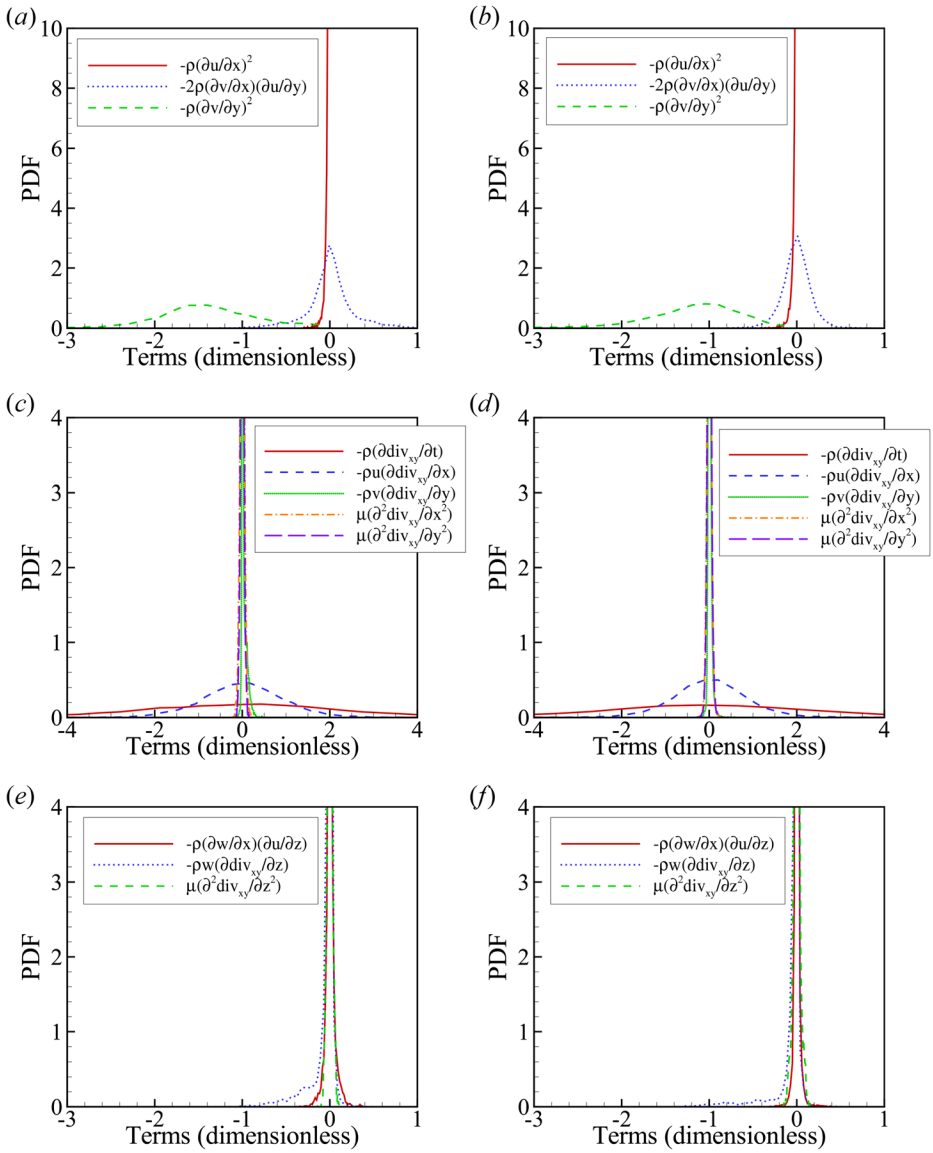

Fig. 20 Probability density function of the terms in Eq. (1). The left column ((*a*), (*c*), (*e*)) and the right column ((*b*), (*d*), and (*f*)) correspond to the case of the counterpart and the experiment, respectively. The terms are normalized by $\rho U_\infty/h^2$.

Given the nonlinearity of the pressure Poisson equation, to estimate the uncertainty of the pressure, Monte Carlo simulation method is applied in this study [34], instead of the uncertainty propagation chain or other analytical methods [35]. Given that the uncertainty of the pressure in the Poisson equation is sourced from the uncertainty of the PIV velocity measurements, thus to estimate the pressure uncertainty, each snapshot of velocity field is superimposed with a noise field on the two components of each displacement vector. The uncertainty of the PIV measurements is estimated to be about 0.1 pixel in displacement in the Davis software of Lavision, which implements the method of [36]. Correspondingly, the noise field is generated with a Gaussian distribution (where the standard deviation is 0.05 pixel and the mean is 0.1 pixel) to approximate the noise in the velocity field. Following that, the velocity with imposed noise is used to obtain the pressure through solving the pressure Poisson equation. In addition to that, the noise of the truncated terms is added by 10% of that of $u\partial \mathrm{div}_{xy}/\partial x$. For each velocity snapshot, this routine is repeated 100 times, and for each of those the noise is newly generated and imposed on the velocity field. This gives the uncertainty of the pressure. This uncertainty is found to be approximately the same for the temporal series at the same spatial location. We then evaluated the sound pressure level (SPL) through the uncertainty propagation chain, and so as the ΔSPL.

References

[1] Morgan, H. G., and Hardin, J. C., 1975, "Airframe Noise-the Next Aircraft Noise Barrier," J. Aircr., **12**(7), pp. 622–624.
[2] Lilley, G., 1998, "A Study of the Silent Flight of the Owl," AIAA Paper No. 1998-2340.
[3] Graham, R. R., 1934, "The Silent Flight of Owls," Aeronaut. J., **38**(286), pp. 837–843.
[4] Hersh, A. S., Soderman, P. T., and Hayden, R. E., 1974, "Investigation of Acoustic Effects of Leading-Edge Serrations on Airfoils," J. Aircr., **11**(4), pp. 197–202.
[5] Cao, H., Zhang, M., Zhang, Y., and Zhou, T., 2021, "A General Model for Trailing Edge Serrations Simulation on Wind Turbine Airfoils," Theory Appl. Mech. Lett., **11**(4), p. 100284.
[6] Jaron, R., Moreau, A., Guérin, S., and Schnell, R., 2018, "Optimization of Trailing-Edge Serrations to Reduce Open-Rotor Tonal Interaction Noise," ASME J. Fluids Eng., **140**(2), p. 021201.
[7] Jaworski, J. W., and Peake, N., 2013, "Aerodynamic Noise From a Poroelastic Edge With Implications for the Silent Flight of Owls," J. Fluid Mech., **723**, pp. 456–479.
[8] Jaworski, J. W., and Peake, N., 2013, "Parametric Guidance for Turbulent Noise Reduction From Poroelastic Trailing Edges and Owls," AIAA Paper No. 2013-2007.
[9] Clark, I. A., Daly, C. A., Devenport, W., Alexander, W. N., Peake, N., Jaworski, J. W., and Glegg, S., 2016, "Bio-Inspired Canopies for the Reduction of Roughness Noise," J. Sound Vib., **385**, pp. 33–54.
[10] Gonzalez, A., Glegg, S. A., Hari, N., and Devenport, W. J., 2019, "Fundamental Studies of the Mechanisms of Pressure Shielding," AIAA Paper No. 2019-2403.
[11] Pope, S. B., 2000, *Turbulent Flows*, Cambridge University Press, New York.
[12] Fröhlich, J., and von Terzi, D., 2008, "Hybrid LES/RANS Methods for the Simulation of Turbulent Flows," Prog. Aerosp. Sci., **44**(5), pp. 349–377.
[13] Bai, K., and Katz, J., 2014, "On the Refractive Index of Sodium Iodide Solutions for Index Matching in PIV," Exp. Fluids, **55**(4), p. 1704.
[14] White, F. M., 2006, *Viscous Fluid Flow*, McGraw-Hill, New York.
[15] Schlichting, H., and Gersten, K., 2017, *Boundary-Layer Theory*, Springer, Heidelberg.
[16] Fellouah, H., and Pollard, A., 2009, "The Velocity Spectra and Turbulence Length Scale Distributions in the Near to Intermediate Regions of a Round Free Turbulent Jet," Phys. Fluids, **21**(11), p. 115101.
[17] Doron, P., Bertuccioli, L., Katz, J., and Osborn, T. R., 2001, "Turbulence Characteristics and Dissipation Estimates in the Coastal Ocean Bottom Boundary Layer From PIV Data," J. Phys. Oceanogr., **31**(8), pp. 2108–2134.
[18] Xu, D., and Chen, J., 2013, "Accurate Estimate of Turbulent Dissipation Rate Using PIV Data," Exp. Therm. Fluid Sci., **44**, pp. 662–672.
[19] Raffel, M., Willert, C. E., Wereley, S. T., and Kompenhans, J., 2007, *Particle Image Velocimetry: A Practical Guide*, Springer, Berlin.
[20] Zhang, Z., Cui, G., and Xu, C., 2002, "Modern Turbulence and New Challenges," Acta Mech. Sin., **18**, pp. 309–327.
[21] de Kat, R., van Oudheusden, B. W., and Scarano, F., 2008, "Instantaneous Planar Pressure Field Determination Around a Square-Section Cylinder Based on Time-Resolved stereo-PIV," AIAA Paper No. 2009-4043.
[22] van Oudheusden, B. W., 2013, "PIV-Based Pressure Measurement," Meas. Sci. Technol., **24**(3), p. 032001.
[23] Kuperman, W. A., and Roux, P., 2007, *Underwater Acoustics, Springer Handbook of Acoustics*, Springer, New York, pp. 149–204.
[24] Morilhat, S., Chedevergne, F., and Simon, F., 2019, "A Unified Methodology to Evaluate the Radiated Noise Due to Turbulent Boundary Layer Flows," ASME J. Fluids Eng., **141**(6), p. 061201.
[25] Gonzalez, A. J., 2019, "A Computational Analysis of Bio-Inspired Modified Boundary Layers for Acoustic Pressure Shielding in a Turbulent Wall Jet," Master's thesis, Florida Atlantic University, Boca Raton, FL.
[26] Lee, Y.-T., Blake, W. K., and Farabee, T. M., 2005, "Modeling of Wall Pressure Fluctuations Based on Time Mean Flow Field," ASME J. Fluids Eng., **127**(2), pp. 233–240.
[27] Remmler, S., Christophe, J., Anthoine, J., and Moreau, S., 2010, "Computation of Wall Pressure Spectra From Steady Flow Data for Noise Prediction," AIAA J., **48**(9), pp. 1997–2007.
[28] Slama, M., Leblond, C., and Sagaut, P., 2018, "A Kriging-Based Elliptic Extended Anisotropic Model for the Turbulent Boundary Layer Wall Pressure Spectrum," J. Fluid Mech., **840**, pp. 25–55.
[29] Gao, D., Chang, X., Chen, G., and Chen, W., 2022, "Fluid Dynamics Behind a Circular Cylinder Embedded With an Active Flapping Jet Actuator," ASME J. Fluids Eng., **144**(2), p. 021301.
[30] Kutz, J. N., Brunton, S. L., Brunton, B. W., and Proctor, J. L., 2016, *Dynamic Mode Decomposition: Data-Driven Modeling of Complex Systems*, Society for Industrial and Applied Mathematics, Philadelphia, PA.
[31] Rising, C. J., Reyes, J., and Ahmed, K. A., 2022, "Characteristics of a Single Sensor Fiber-Coupled Three-Dimensional Particle Image Velocimetry for Reacting Flow-Fields," ASME J. Fluids Eng., **144**(1), p. 011502.
[32] Zhang, T., Huang, G., Yin, J., Zhang, Z., Wang, D., Sun, Y., and Liao, Y., 2022, "Investigation on Swirl Instability in a Vane-Type Separator With Tomographic Particle Image Velocimetry," ASME J. Fluids Eng., **144**(5), p. 051402.
[33] Wang, X., Zhang, J., Huang, Z., Wang, L., Li, W., and Lan, G., 2023, "Large Eddy Simulation on the Cavitation Flow and Noise Characteristics of a NACA0009 Hydrofoil With Different Tip Clearance Sizes," ASME J. Fluids Eng., **145**(1), p. 011204.
[34] Papadopoulos, C. E., and Yeung, H., 2001, "Uncertainty Estimation and Monte Carlo Simulation Method," Flow Meas. Instrum., **12**(4), pp. 291–298.
[35] ISO, 2008, "ISO/IEC Guide 98-3:2008 Uncertainty of Measurement—Part 3: Guide to the Expression of Uncertainty in Measurement (GUM:1995)," Standard, International Organization for Standardization, Geneva, Switzerland.
[36] Wieneke, B., 2015, "PIV Uncertainty Quantification From Correlation Statistics," Meas. Sci. Technol., **26**(7), p. 074002.